Journal of Colloid and Interface Science 566 (2020) 248–256

Contents lists available at ScienceDirect

Journal of Colloid and Interface Science

journal homepage: www.elsevier.com/locate/jcis

Efficient electrochemical biosensing of hydrogen peroxide on bimetallic $Mo_{1-x}W_xS_2$ nanoflowers

Yijin Shu [a], Wenbiao Zhang [a], Xing Yin [a], Lingli Zhang [b], Yang Yang [a], Dong Ma [b], Qingsheng Gao [a,*]

[a] College of Chemistry and Materials Science, Jinan University, Guangzhou 510632, China
[b] Key Laboratory of Biomaterials of Guangdong Higher Education Institutes, Department of Biomedical Engineering, Jinan University, Guangzhou 510632, China

HIGHLIGHTS

- Bimetallic $Mo_{1-x}W_xS_2$ identifies composition-dependent H_2O_2 sensing associated with intermediate bindings.
- The optimal $Mo_{0.75}W_{0.25}S_2$ accomplishes outstanding performance in H_2O_2 sensing.
- The $Mo_{0.75}W_{0.25}S_2$ distinguishes cancer cells via monitoring endogenous H_2O_2.

GRAPHICAL ABSTRACT

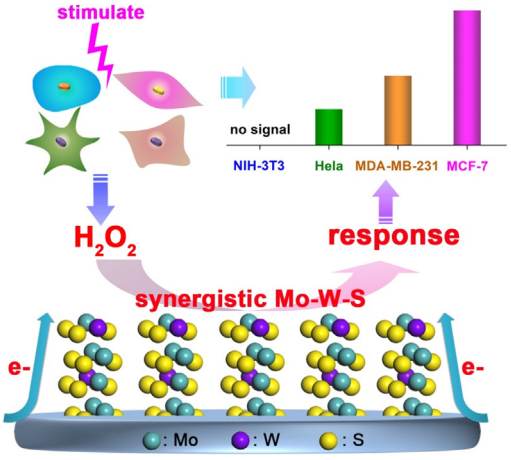

ARTICLE INFO

Article history:
Received 31 October 2019
Revised 18 January 2020
Accepted 22 January 2020
Available online 23 January 2020

Keywords:
Electrochemical biosensor
H_2O_2 detection
Transition-metal dichalcogenides
Electronic configurations
Intermediate bindings

ABSTRACT

Two-dimensional transition-metal dichalcogenides can serve as emerging biosensing platforms after rational structural optimization. Herein, we develop a series of $Mo_{1-x}W_xS_2$ and investigate the composition-dependent sensing of hydrogen peroxide (H_2O_2). Among them, the $Mo_{0.75}W_{0.25}S_2$ affords high sensitivity (1290 μA mM^{-1} cm^{-2}), good selectivity, and wide applicable concentration range (4×10^{-1}–1.0×10^4 μM). As indicated by theoretical investigations, such prominent performance stems from the bimetallic electronic configurations and the enhanced *OH binding on surface. Moreover, the $Mo_{0.75}W_{0.25}S_2$ is capable of monitoring trace amounts of H_2O_2 released from normal cells and various cancer cells, which provides efficient cell detection for clinical diagnosis. In addition, the composition-dependence, as a result of electronic modulation on $Mo_{1-x}W_xS_2$ surface, is further evidenced on electrocatalytic hydrogen evolution reaction, which highlights the promise in sensing and electrocatalysis that share similar electrochemical fundamentals.

1. Introduction

Electrochemical detection of biomarkers (e.g. small molecules, DNA, proteins, cells, etc.) *in vitro* and *in vivo* is promising in real-time monitoring, clinical diagnosis and pathophysiology [1–4].

* Corresponding author.
E-mail address: tqsgao@jnu.edu.cn (Q. Gao).

https://doi.org/10.1016/j.jcis.2020.01.083
0021-9797/

They feature obvious advantages, including robustness, easy miniaturization, excellent detection limits, and also small analyte volumes, in comparison with other techniques (e.g., enzyme-linked immunosorbent assay, mass spectrometry, northern blot, etc.) that require technically complex equipment or time-consuming manipulation [5]. As a typical representative of reactive oxygen species (ROS) in biological systems, hydrogen peroxide (H_2O_2) plays a key role in cell proliferation and death, response to chronic diseases, and intracellular signaling transduction [6–8]. For instance, the concentration of H_2O_2 in tumor area is typically higher than that in normal tissue [9,10]. Thus rapid, accurate, and reliable determination of H_2O_2 shows practical importance in biological analyses. In H_2O_2 sensing, nanomaterials based non-enzymatic electrochemical biosensors can surmount the inherent problems of enzyme biosensors, such as rigorous storage conditions and short period of validity [11,12]. Rational structural optimization is anticipated to improve the sensing performance of non-enzymatic nanomaterials, regarding that H_2O_2 sensing relies on the electrochemical redox processes of H_2O_2 [13]. Non-enzymatic materials serve as electrocatalysts to boost the oxidation/reduction, thereby amplifying current response.

Two-dimensional (2D) transition-metal dichalcogenides (TMDs) have attracted attentions in biosensing due to their unique electronic/optical properties, versatile chemistry and easy surface-functionalization [14–17]. In particular, molybdenum disulfide (MoS_2) based nanostructures are functional segments to detect proteins, DNA, cancer cells, cellular metabolism products, etc. [18–20]. In H_2O_2 sensing, conventional MoS_2 however suffers from low sensitivity on un-optimized surface. Therefore, many efforts in engineering particle size [21], edge-site exposure [22] and interlayer structures [23] have been made. Besides, heteroatom doping is an alternative approach to promote sensing performance due to effective modification on electronic configurations. For instance, Ni [24,25], Cu [26], Ag [27] and N [28] are available dopants. However, such foreign elements with quite different atomic size and chemical properties from Mo or S usually destroy the parent lattices at high doping content, leading to unsatisfactory sensing response [29]. As congeners, W has the same valence electrons and chemical properties with Mo, and their disulfides share the similar layered structures. The solid-solution alloy phase of Mo-W-S will enable the precise and adequate electronic regulation toward optimal performance [30].

Recently, our work for the first time discovered that expanding the interlayer spacing of MoS_2 can boost the electrochemical biosensing performance due to electronic regulation [23]. However, the effects of heteroatom doping and solid-solution-alloy have not been studied in this promising system, which are anticipated to bring further improvement in applications. Herein, we fabricate a series of $Mo_{1-x}W_xS_2$ and investigate their composition-dependent sensing for H_2O_2. The $Mo_{0.75}W_{0.25}S_2$ affords high sensitivity (1290 μA mM^{-1} cm^{-2}), good selectivity, and wide applicable concentration range (4×10^{-1}–1.0×10^4 μM) for H_2O_2 detection, superior to MoS_2, WS_2 and other counterparts with a high W content. As further confirmed by theoretical investigations, such performance stems from the enhanced *OH binding on surface. However, further increasing W content in $Mo_{1-x}W_xS_2$ (x > 0.50) will lead to coarsened products that lose a large part of active edge-sites, which accounts for the prohibited performance. Furthermore, the $Mo_{0.75}W_{0.25}S_2$ is capable of monitoring trace amounts of H_2O_2 released from normal cells and different cancer cells, which provides efficient cell detection for clinical diagnosis. The above composition-dependence, as a result of the electronic modulation on $Mo_{1-x}W_xS_2$, is also evidenced on electrocatalytic hydrogen evolution reaction (HER), highlighting the universal promotion in sensing and electrocatalysis that share similar electrochemical fundamentals.

2. Experimental section

2.1. Materials and reagents

Ammonium heptamolybdate tetrahydrate ($(NH_4)_6Mo_7O_{24}\cdot 4H_2O$, 99.5%, Aladdin), sodium tungstate dihydrate ($Na_2WO_4\cdot 2H_2O$, 99%, Aladdin), thiourea (99%, Aladdin), *N*,*N*-dimethylformamide (DMF, 99.5%, Aladdin), hydrogen peroxide (30%, Guangzhou chemical reagent factory) and phosphate-buffered saline (PBS, 0.1 M, pH = 7.4, Gibco) were used for experiments as received. Phorbol 12-myristate 13-acetate (PMA, 98%), catalase (5000 U mg^{-1}) and Nafion solution (5 wt% in lower aliphatic alcohols and water) were purchased from Sigma-Aldrich. All chemicals were of analytical grade and used as received without further purification. All aqueous solutions were prepared using ultrapure water (>18 MΩ).

2.2. Physical characterization

Scaning electronic microscopy (SEM) was taken on a ZEISS ULTRA55. Transition electronic microscopy (TEM), energy dispersive spectroscopy (EDS) and elemental mapping were conducted on a JEOL JEM 2100F. X-ray diffraction (XRD) was performed on Bruker D8 Advance diffractometer using Cu Kα radiation (λ = 1.54056 Å). Raman spectra were recorded on a laser confocal Raman microspectrometer (HR-800, Horiba Jobin Yvon, Ltd.), with an excitation laser wavelength of 532 nm. X-ray photoelectron spectroscopy (XPS) was processed on a Thermo scientific (Escalab 250Xi), using C 1s (284.6 eV) as a reference.

2.3. Material synthesis

The synthesis of $Mo_{1-x}W_xS_2$, MoS_2 and WS_2 nanoflowers was conducted via a simple one-pot hydrothermal process. Typically, 5.0 mL of distilled water and 5.0 mL of DMF were mixed as a solvent. A varied amount of $(NH_4)_6Mo_7O_{24}\cdot 4H_2O$ and $Na_2WO_4\cdot 2H_2O$ (total n_{Mo+W} is fixed as 2 mmol) and 1.525 g of thiourea (20 mmol) were dissolved into the above solvent, which was then stirred for 30 min to get a clean solution. The solution was transferred to a Teflon-lined stainless steel autoclave. After reaction at 240 °C for 3 h, the product was collected by centrifugation, washed with ethanol and water at least 3 times, and dried at 50 °C overnight. MoS_2 or WS_2 is obtained by adding only molybdenum or tungsten sources, respectively.

2.4. Electrochemical measurement

Electrochemical test was conducted with a conventional three-electrode system on a CHI 650E electrochemical workstation (Chenhua Instruments Shanghai Co., Ltd, China). A Ag/AgCl (3 M KCl) electrode and a platinum wire were used as the reference and counter electrodes, respectively.

The preparation of working electrodes is as follow. Prior to modification, a bare rotating disk electrode (RDE) or glassy carbon electrode (GCE) was polished with 0.3 and 0.03 μm alumina powder on a polishing cloth to obtain a mirror like surface. 4 mg of $Mo_{1-x}W_xS_2$ and 40 μL of 5 wt% Nafion solution were dispersed in 1 mL of 4:1 vol/vol deionzed water–ethanol mixed solvent, which was vigorously sonicated for at least 30 min to generate a homogeneous ink. Then, 15 μL (5 μL in GCE case) of the ink was loaded onto a RDE (5 mm diameter, 0.196 cm^2) or a GCE (0.07 cm^2), and dried naturally in air. Electrochemical sensing H_2O_2 were performed at 25 °C in 0.1 M PBS buffer, and electrochemical hydrogen evolution was performed in 0.5 M H_2SO_4 solution.

2.5. Electrochemical determination of intracelluar H_2O_2 released from living cells

MDA-MB-231 (human breast adenocarcinoma cell line), MCF-7 (human breast cancer cells) and Hela (human cervical cancer cells) were obtained from Southern Medical University (Guangzhou, China). MDA-MB-231 cells were incubated in the flask (75 cm^2) in Roswell Park Memorial Institute (RPMI) Medium 1640 basic containing 10% FBS (fetal bovine serum) and 1% antibiotics overnight (penicillin streptomycin, 1×10^4 U/mL), plated in a 5% CO_2 and 95% air at 37 °C. MCF-7 and Hela were cultured in Dulbecco's modified Eagle medium (DMEM) containing 10% FBS, 100 U mL^{-1} penicillin, and 100 mg mL^{-1} streptomycin at 37 °C in a 5% CO_2 environment. Cancer cells were digested with 0.25 wt% trypsin at 37 °C for 120 s and separated from the culture medium by centrifugation (1000 rpm) for 5 min, then washed with PBS (0.01 M, pH 7.4) for three times, and finally suspended in PBS to 5×10^6 cells mL^{-1}.

The 1 mL cancer cells were mixed with 49 mL 0.1 M PBS buffer to reach its concentration of 1×10^5 cells mL^{-1}. PMA was employed as the stimulant for intracellular H_2O_2 release. To detect H_2O_2 released from cells, the response of amperometric current-time plot was performed on the $Mo_{1-x}W_xS_2$/RDEs.

2.6. Theoretical calculations

The OH adsorption energy ($\triangle E_{OH}$) calculations on the edge of MoS_2, $Mo_{0.75}W_{0.25}S_2$ and $Mo_{0.50}W_{0.50}S_2$ were carried out by using Cambridge Sequential Total Energy Package (CASTEP) module in Material Studio. And $\triangle E_{OH}$ was calculated as:

$$\Delta E_{OH} = E_{(slab+adsorbate)} - E_{(slab)} - E_{(adsorbate)}$$

where $E_{(slab + adsorbate)}$, $E_{(slab)}$ and $E_{(adsorbate)}$ were the total energy of slab with adsorbate, the energy of pure slab/facet and the energy of adsorbate (OH) in the gas phase, respectively.

The exchange correlation energy was described by the generalized gradient approximation (GGA) with the Perdew-Burke-Ernzerhof (PBE) functional [31,32]. The kinetic energy cutoff for the plane-waves expansion was 450 eV. The self-consistent field (SCF) tolerance was 1×10^{-6} eV. The Brillouin zone was sampled by $3 \times 3 \times 1$ k-points. MoS_2, $Mo_{0.75}W_{0.25}S_2$ and $Mo_{0.50}W_{0.50}S_2$ crystal structure with an expanded interlayer spacing of 9.4 Å adopts a hexagonal crystal structure, using $2 \times 2 \times 1$ supercell. Vacuum thickness of 15 Å was chosen to simulate the surface properties.

3. Results and discussion

3.1. Characterization of $Mo_{1-x}W_xS_2$

A series of $Mo_{1-x}W_xS_2$ is fabricated via a one-pot hydrothermal process with various feeding molar ratios of Mo/W. The Mo/W ratio in products determined by EDS is consistent with the feeding one. As depicted in the XRD patterns (Fig. 1a), all the $Mo_{1-x}W_xS_2$ shows an obviously down-shifting (0 0 2) peak at 2θ = 9.35° (d ≈ 0.94 nm), in comparison with hexagonal MoS_2 (JCPDS No.: 37-1492) and WS_2 (JCPDS No.: 08-0237), but retains other peaks such as (0 1 0) and (1 1 0) without shift. This indicates an interlayer expanded structure along the [0 0 2] direction. According to our and other groups' previous reports [23,33], the strong interactions between MoS_2 monolayers and excessive thiourea or DMF derivatives will expand the typical (0 0 2) d-spacing (0.62 nm) of MoS_2 to a large one (e.g., 0.94 nm). As the W content increases, the diffraction peaks become sharp and narrow, indicating the enlarged and thickened nanosheets. In Raman spectra (Fig. 1b), the MoS_2 exhibits two distinct bands at 379.7 and 402.9 cm^{-1}, corresponding to the E^1_{2g} (in-plane) and A_{1g} (out of plane) vibrations, respectively [34]. The peaks at 349.5, 354.8 and 415.3 cm^{-1} are observed on WS_2, which can be ascribed to 2 LA(M) (the second-order mode of longitudinal acoustic phonon), E^1_{2g} (in-plane) and A_{1g} (out of plane), respectively [35]. With increasing W content, the E^1_{2g} band shifts to lower wavenumbers while A_{1g} mode to higher range. This variation is in accordance with the evidenced spectral evolution in previous reports, and probably due to strong interactions between Mo and W [29].

SEM investigation clearly reveals the flower-like samples consisting of stacked nanosheets (Fig. 2). The MoS_2 nanoflowers present a small size (~200 nm), and the nanosheets are thin (Fig. 2a). By contrast, the WS_2 assembled by thicker nanoplates is as large as several microns (Fig. 2f). This suggests the different growth of MoS_2 and WS_2 crystals. In the case of $Mo_{1-x}W_xS_2$, introducing a small amount of W has slight influences on the size (e.g., $Mo_{0.75}W_{0.25}S_2$ and $Mo_{0.50}W_{0.50}S_2$), but high x in $Mo_{0.33}W_{0.67}S_2$ and $Mo_{0.20}W_{0.80}S_2$ leads to the coarsened products. Obviously, the formers will be beneficial for sensing application.

TEM observation shows that the flower-like $Mo_{0.75}W_{0.25}S_2$, as a model sample, consists of thin nanosheets (Fig. 3a). And the high-resolution TEM (HR-TEM) identifies the lattice fringes of 0.94 and 0.27 nm on the nanosheets (Fig. 3b). The former is ascribed to the expanded (0 0 2) interlayers, agreeing with that of XRD results (Fig. 1a). Such value keeps the same in single-component MoS_2 and

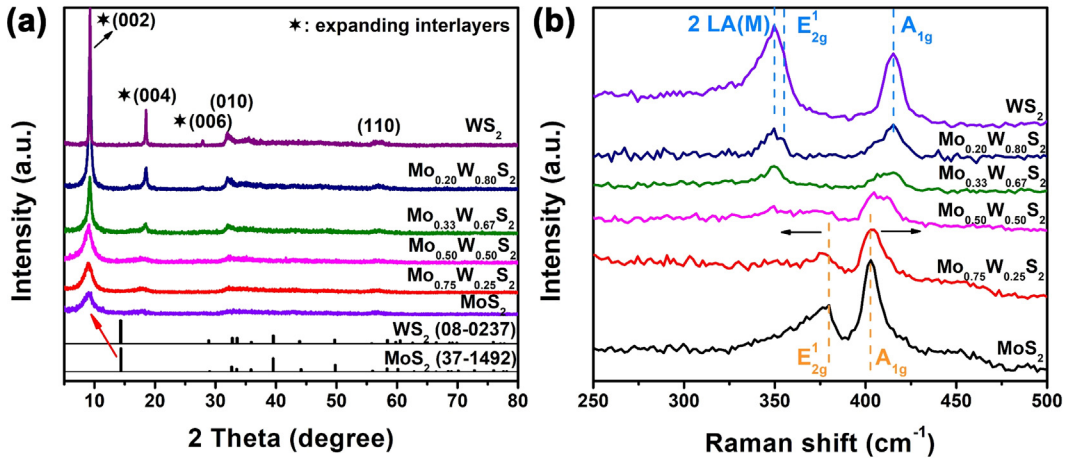

Fig. 1. (a) XRD patterns and (b) Raman spectra of MoS_2, WS_2 and $Mo_{1-x}W_xS_2$.

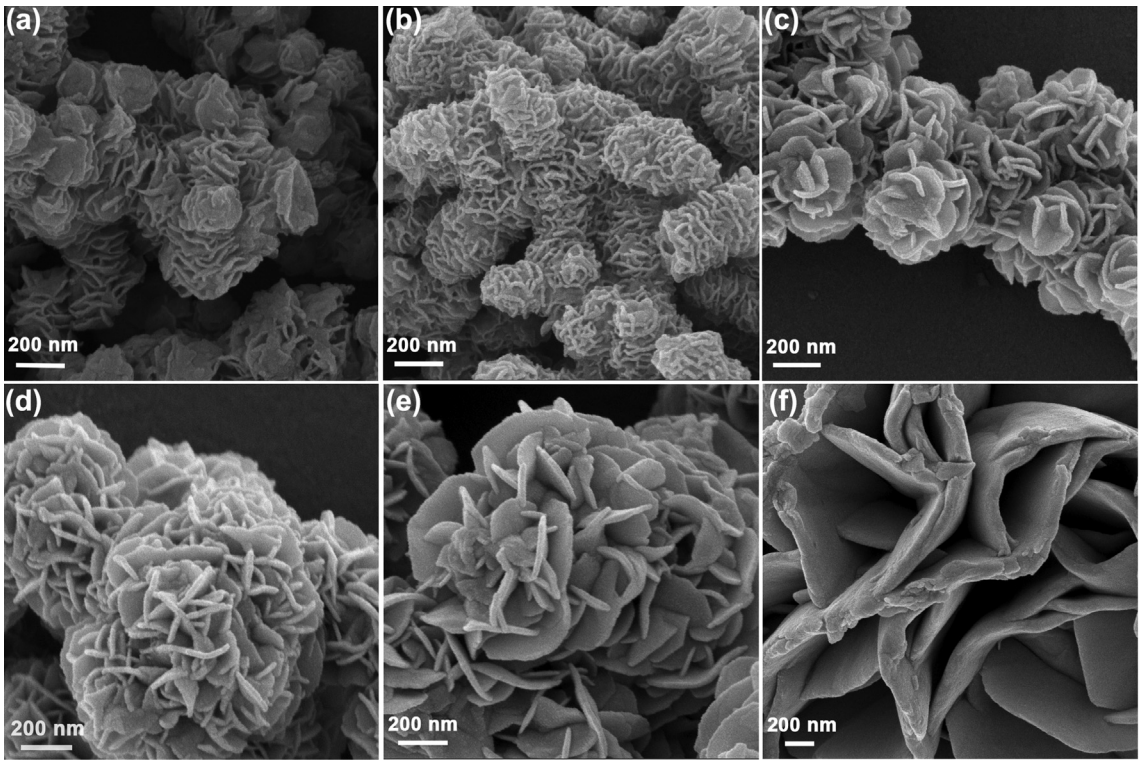

Fig. 2. SEM images of (a) MoS_2, (b) $Mo_{0.75}W_{0.25}S_2$, (c) $Mo_{0.50}W_{0.50}S_2$, (d) $Mo_{0.33}W_{0.67}S_2$, (e) $Mo_{0.20}W_{0.80}S_2$ and (f) WS_2.

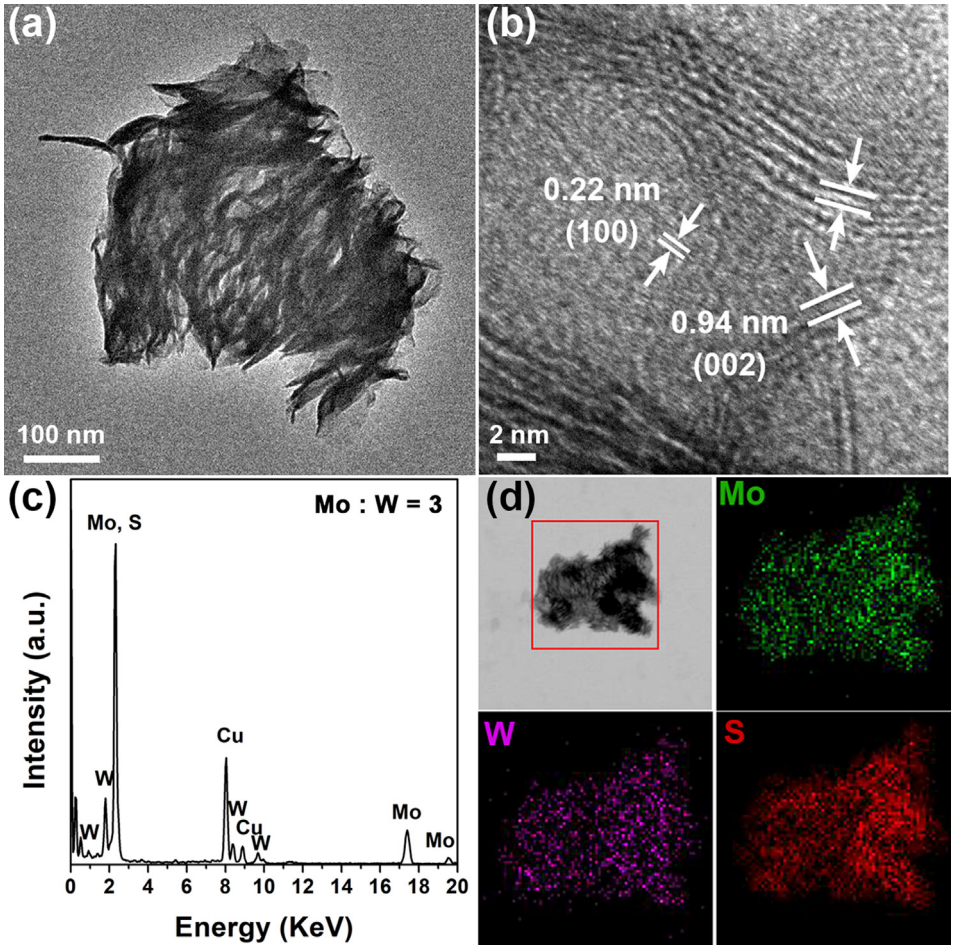

Fig. 3. (a) TEM and (b) HR-TEM images, (c) EDS pattern and (d) corresponding elemental mapping of the $Mo_{0.75}W_{0.25}S_2$ nanoflowers.

WS_2 (Figs. S1 and S2 in Supplementary materials). And the latter can be assigned to the (0 1 0) of $Mo_{0.75}W_{0.25}S_2$, which is non-affected in interlayer expanded sulfides. Moreover, the EDS attached on TEM shows the signals of Mo, W, S, C and N, and the additional peak for Cu is associated with the background of support grid (Fig. 3c). The Mo/W atomic ratio is confirmed as 3.0, in accordance with the feeding ratio. Elemental mapping further presents the uniform distribution of Mo, W and S on the nanosheets (Fig. 2d), indicating the uniform integration of W and Mo in $Mo_{1-x}W_xS_2$.

XPS survey spectra reveal the surface composition of MoS_2, $Mo_{1-x}W_xS_2$ and WS_2 (Fig. S3 in Supplementary materials). The elements of Mo, W and S are observed in $Mo_{1-x}W_xS_2$, while W is absent in MoS_2, and Mo in WS_2. The chemical states of the above elements are further analyzed. As showed in Fig. 4a, the Mo profile of MoS_2 can be deconvoluted into five peaks. The peak at 225.9 eV corresponds to the S 2 s, and the ones at 228.7 and 232.1 eV are ascribed to the Mo $3d_{5/2}$ and $3d_{3/2}$ of Mo^{4+} in MoS_2, respectively [36,37]. The couple at 232.9 and 235.5 eV is ascribed to the small amount of Mo^{6+} that is due to the slight oxidation of MoS_2 in air ambience. Such surface oxidation is depressed in bimetallic $Mo_{1-x}W_xS_2$, which is helpful to expose more surface active sites. When W proportion increases ($Mo_{0.50}W_{0.50}S_2$, $Mo_{0.33}W_{0.67}S_2$ and $Mo_{0.20}W_{0.80}S_2$), the binding energy of Mo^{4+} affords a red-shift as compared with bare MoS_2. Meanwhile, the W 4f profile of WS_2 can be deconvoluted into two couples (Fig. 4b). The ones at 31.8 and 33.9 eV are related to W^{4+} in WS_2, the other is associated with the W^{6+} of surface oxides [38,39]. With the fixed values for W^{6+}, the couple of W^{4+} in $Mo_{1-x}W_xS_2$ presents a blue-shift with increasing Mo, indicating rich electronic interactions between Mo and W. In addition, the profiles of S 2p keeps consistent in all the above samples (Fig. 4c).

3.2. Electrochemical H_2O_2 sensing on $Mo_{1-x}W_xS_2$

In electrochemical H_2O_2 sensing, the MoS_2, WS_2 and $Mo_{0.75}W_{0.25}S_2$ are modified onto RDEs to measure the electrochemical signals responding to H_2O_2 injection (Fig. 5a). The $Mo_{0.75}W_{0.25}S_2$ affords an obviously increased current in the presence of H_2O_2, and performs more sensitively than bare MoS_2 and WS_2, indicating the promoted sensing due to W doping into MoS_2. Such response is also superior to that on other $Mo_{1-x}W_xS_2$ with different compositions (Fig. S4 in Supplementary materials). More details for H_2O_2 sensing were further assessed by amperometric *i–t* curves in response to H_2O_2 concentration. The test was conducted by successively adding H_2O_2 into a 0.1 M PBS solution, at a working potential of −0.6 V *vs.* Ag/AgCl (3 M KCl). As shown in Fig. 5b, the MoS_2, WS_2 and $Mo_{1-x}W_xS_2$ exhibit satisfactory reproducibility, and all the $Mo_{1-x}W_xS_2$ delivers higher increase in response currents than the mono-metallic disulfides (MoS_2 and WS_2), indicating the synergic enhancement by Mo and W components. Accordingly, Fig. 5c summarizes the average changes of currents responding to injecting H_2O_2. The changes on $Mo_{1-x}W_xS_2$ are more sensitive than that on MoS_2 and WS_2. And the $Mo_{0.75}W_{0.25}S_2$ reaches a maximum increase, indicating the most sensitive response due to the optimal composition. In addition, the sensitive response on the $Mo_{0.75}W_{0.25}S_2$ is also confirmed at a work potential from −0.05 to −0.70 V (Fig. S5 in Supplementary materials).

According to previous reports, the cathodic H_2O_2 sensing proceeds via H_2O_2 reduction to H_2O [13,32]. And the rate-determining step of electrochemical H_2O_2 reduction is the cleavage of O—O bond to form adsorbed *OH, which is correlated with the *OH binding on material surface. In this regard, density functional theoretical (DFT) calculations were conducted to reveal the varied binding energy. The high proportion of W obviously leads to the enlarged size of $Mo_{1-x}W_xS_2$ (e.g., $Mo_{0.33}W_{0.67}S_2$ and $Mo_{0.20}W_{0.80}S_2$), and thus other impacts beyond electronic effects emerge on sensing. Thereby, only the MoS_2, $Mo_{0.75}W_{0.25}S_2$ and $Mo_{0.50}W_{0.50}S_2$ with consistent particle sizes are taken into account. Fig. 5d presents the chemisorption configuration and the binding energy of *OH on the edge (1 0 0). The value on the $Mo_{0.75}W_{0.25}S_2$ is −3.7 eV, more negative than that on MoS_2 and $Mo_{0.50}W_{0.50}S_2$, indicating the stronger binding. This is beneficial for the cleavage of O—O bond during H_2O_2 reduction, and responsible for the sensitive response in H_2O_2 detection.

Fig. 6a shows the *i-t* curve of a $Mo_{0.75}W_{0.25}S_2$ modified RDE upon continuously injecting H_2O_2 at a holding potential of −0.6 V (*vs.* 3 M Ag/AgCl). The electrode responds quickly and achieves a steady current within 3 s. Moreover, in order to investigate the stability of $Mo_{1-x}W_xS_2$ in H_2O_2 condition, the instrument is turn off for 250 s, and then turn on again. The current signal returns to its original level in a short time. The quick and steady

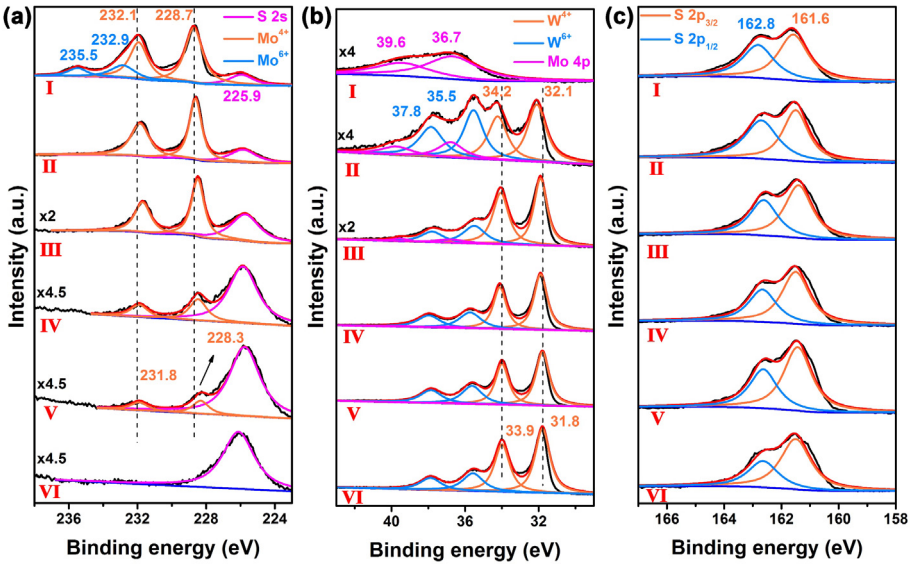

Fig. 4. XPS spectra of (a) Mo 3d, (b) W 4f and (c) S 2p in $Mo_{1-x}W_xS_2$ nanoflowers (I: MoS_2, II: $Mo_{0.75}W_{0.25}S_2$, III: $Mo_{0.50}W_{0.50}S_2$, IV: $Mo_{0.33}W_{0.67}S_2$, V: $Mo_{0.20}W_{0.80}S_2$ and VI: WS_2).

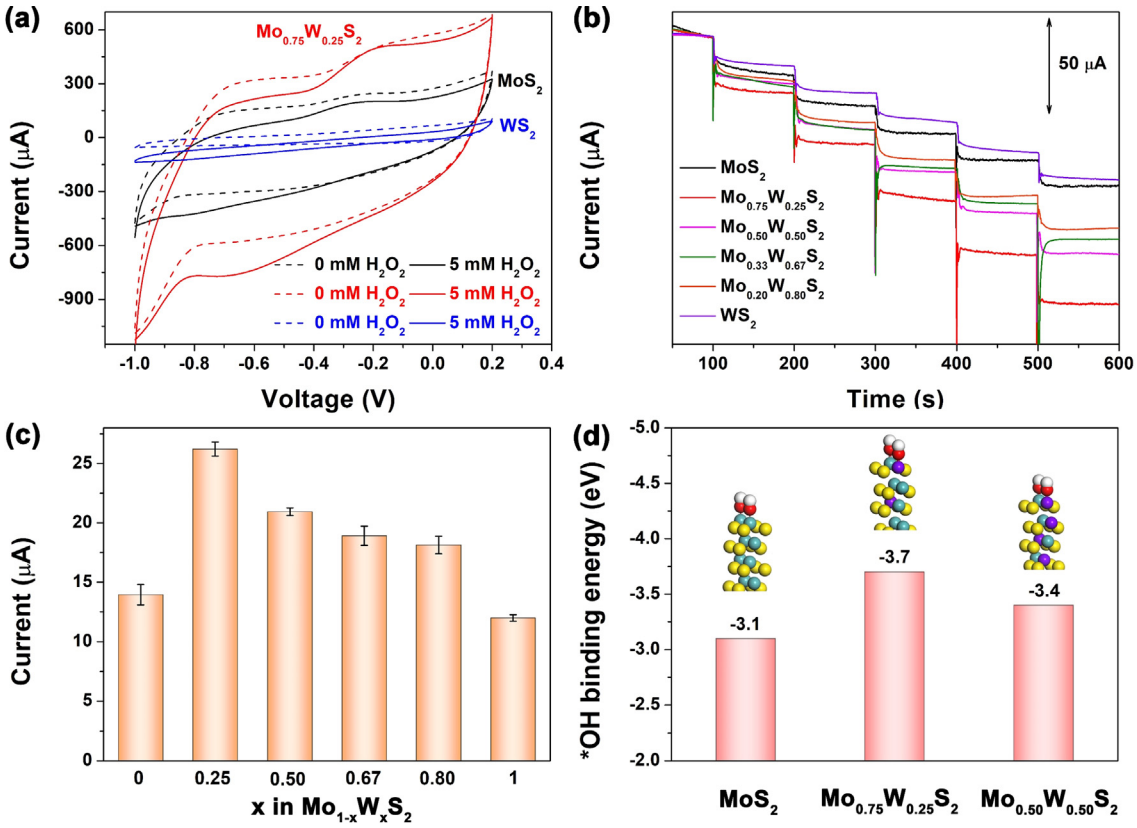

Fig. 5. (a) CVs responses of MoS_2/RDE, WS_2/RDE and $Mo_{0.75}W_{0.25}S_2$/RDE in the absence and presence of 5 mM H_2O_2. (b) Amperometric *i*–*t* curves of $Mo_{1-x}W_xS_2$/RDE in response to the successive addition of 100 μM H_2O_2, and (c) the corresponding current variation associated with x in $Mo_{1-x}W_xS_2$. (d) Chemisorption configuration (S: yellow, Mo: wathet blue, W: purple, O: red, and H: white) and binding energy of *OH on the edge of MoS_2, $Mo_{0.75}W_{0.25}S_2$ and $Mo_{0.50}W_{0.50}S_2$. (For interpretation of the references to color in this figure legend, the reader is referred to the web version of this article.)

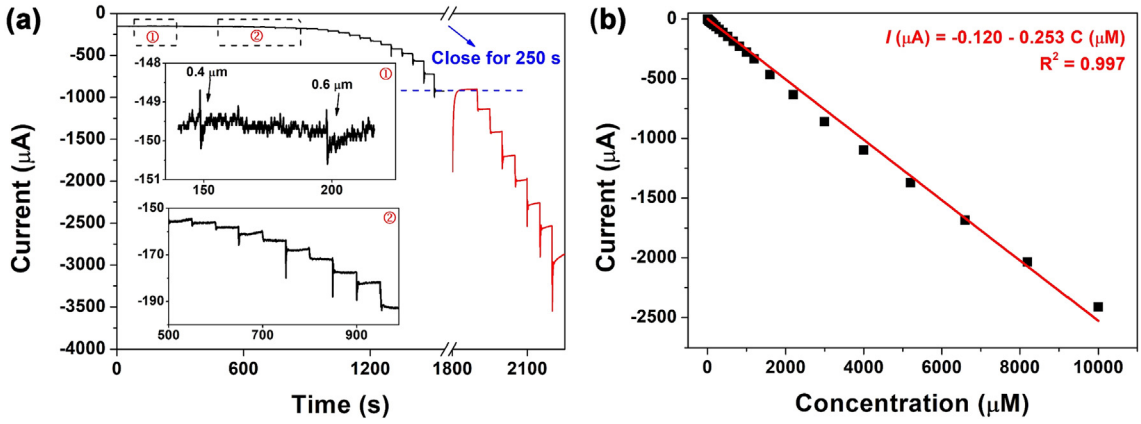

Fig. 6. (a) Amperometric response of a $Mo_{0.75}W_{0.25}S_2$/RDE to dropwise adding H_2O_2, and (b) calibration curve of current *vs*·H_2O_2 concentration.

response is possibly related to the fast H_2O_2 reduction on the edge-sites of $Mo_{0.75}W_{0.25}S_2$. The corresponding calibration curve between current response and H_2O_2 concentration in Fig. 6b gives the regression equation of I (μA) = −0.253 C_{H2O2}(μM) − 0.120 (R^2 = 0.997) in a wide linear range of 4×10^{-1}–1.0×10^4 μM. Calculated from the slope of equation, the sensor shows a high sensitivity of 1290 μA mM^{-1} cm^{-2}. The limit of detection (LOD) of this sensor is calculated as 0.3 μM through the formula: LOD = $3S_b/S$ (Where S_b is standard deviation of blank signal, and S is sensitivity). Our previously developed MoS_2 with expanded interlayers could give higher sensitivity and lower LOD, but its sensitivity obviously decreased at high H_2O_2 concentration [23], showing narrow applicable range in comparison with the $Mo_{0.75}W_{0.25}S_2$ herein. This is possibly associated with the different conditions in hydrothermal synthesis. To study the composition-dependence of $Mo_{1-x}W_xS_2$, reducible DMF was used as the reducing agent and co-solvent to ensure the formation of tungesten sulfides. In further comparison with recently reported materials, the $Mo_{0.75}W_{0.25}S_2$ performs at a high level (Table S1 in Supplementary materials). Its sensitivity or LOD outperforms those even involving enzymes or precious metals. As indicated, rational engineering on TMDs can reach the outstanding sensing performance even free from enzymes and precious metals, which will undoubtedly promote the cost-efficiency of sensing materials in practical use.

Before being applied to real samples, the sensing selectivity of the $Mo_{0.75}W_{0.25}S_2$ was concerned, because the capability of recognizing target molecules in complex biological environment is practically important. Possible interferences including L-cysteine, glucose, ascorbic acid, dopamine, uric acid and inorganic salt that usually co-exist with H_2O_2 in body fluid are added sequentially during measuring the current response upon injecting H_2O_2. As shown in Fig. 7a, the $Mo_{0.75}W_{0.25}S_2$ delivers negligible change, and the subsequent current response to H_2O_2 keep the same intensity as the case free from interferents. This test confirms the good tolerance of $Mo_{0.75}W_{0.25}S_2$ to various interferences.

H_2O_2 plays important roles in cellular processes, and the concentration of H_2O_2 varies with the type and state of cells. For example, the concentration of H_2O_2 is higher in tumor area than that in normal tissue, due to fast oxygen metabolism and unlimited proliferation of cancer cells [9]. Thereby, we can detect and monitor the change of H_2O_2 concentration, and then distinguish these cells. PMA was introduced as stimulant for H_2O_2 release, and the generated H_2O_2 was then irreversibly decomposed after adding catalase. Herein, the optimal $Mo_{0.75}W_{0.25}S_2$ is employed to detect H_2O_2 level in living cancer cells, i.e., MCF-7 (human breast cancer cells), MB-MDA-231 (human breast cancer cells) and Hela cells (human

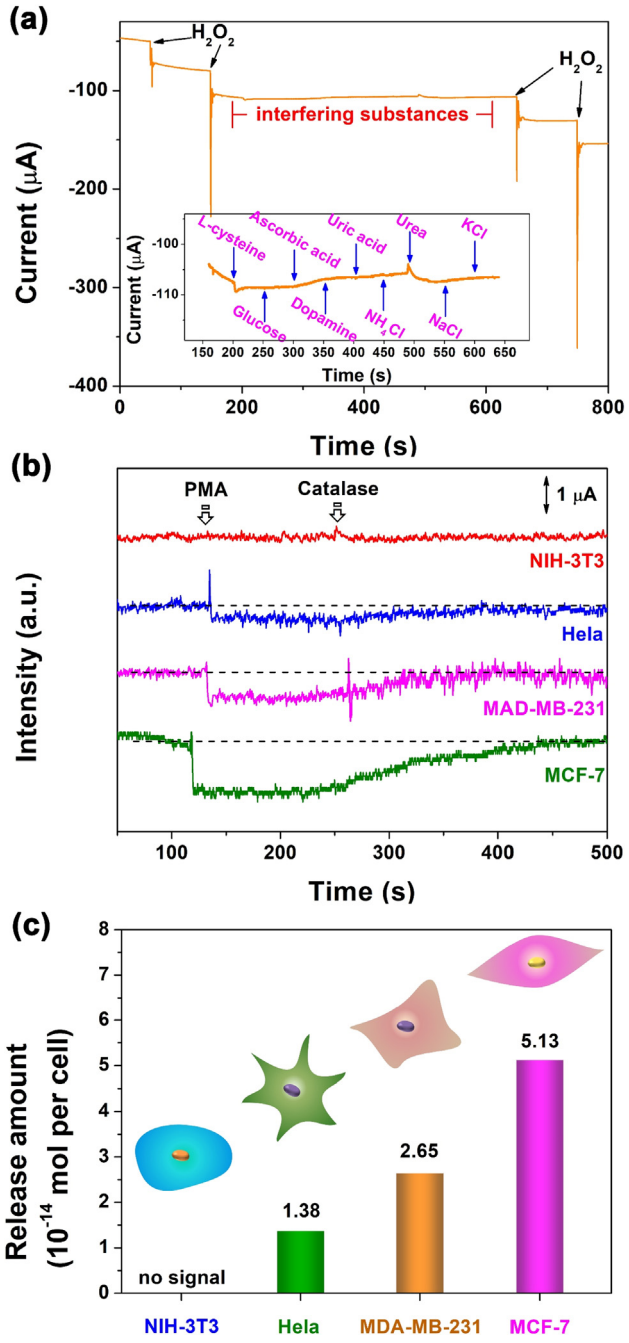

Fig. 7. (a) *i–t* curves on a $Mo_{0.75}W_{0.25}S_2$/RDE responding to H_2O_2 (100 μM) in the presence of various interfering substances (1000 μM). (b) Current response on $Mo_{0.75}W_{0.25}S_2$/RDEs to injecting PMA and catalase into 0.1 M PBS with various cells, and (c) the corresponding amount of H_2O_2 released from cells.

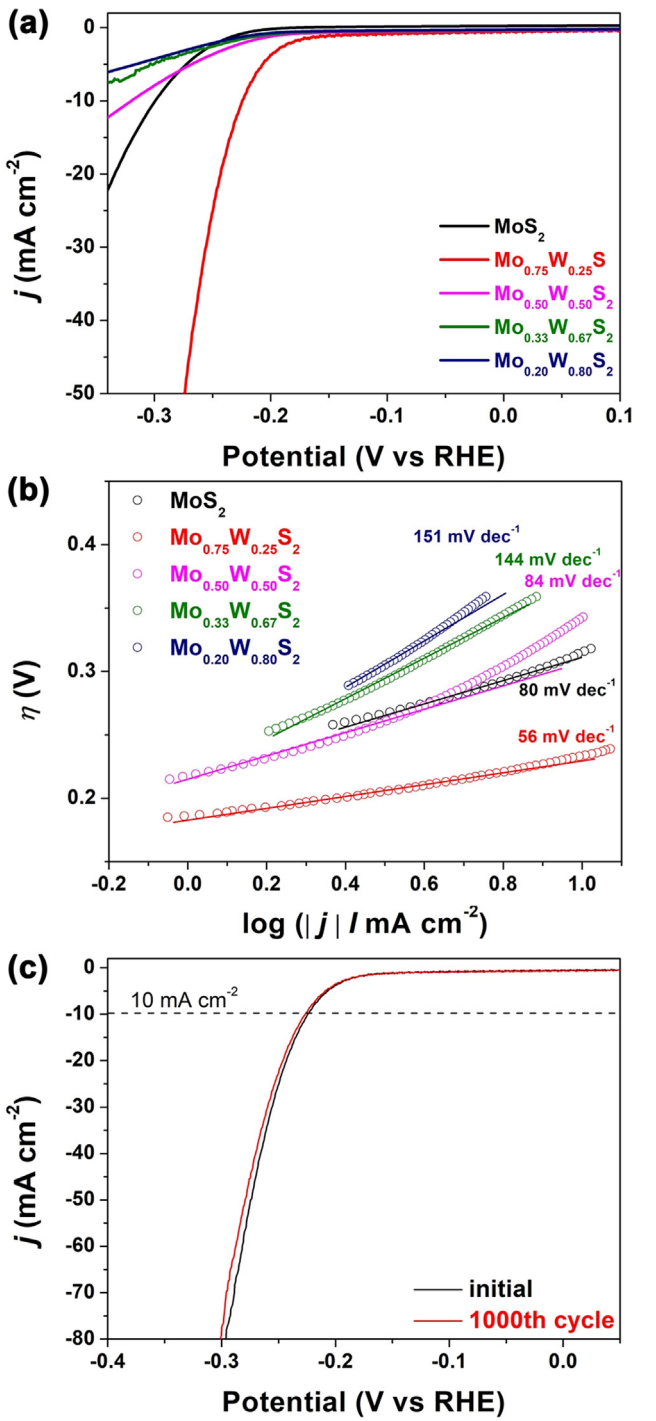

Fig. 8. (a) Polarization curves and (b) corresponding Tafel plots of MoS_2 and $Mo_{1-x}W_xS_2$ modified GCEs in 0.5 M H_2SO_4. (c) Stability test of $Mo_{0.75}W_{0.25}S_2$/GCE in 0.5 M H_2SO_4.

cervical cancer cells). As shown in Fig. 7b, in the presence of the above cells, quick current responses are observed after injecting PMA, and the current decreases to a background level as catalase is introduced, because catalase can irreversibly decompose H_2O_2 to O_2 and H_2O. It's suggested that the current response is due to H_2O_2 released from cancer cells. By contrast, non-cancerous NIH-3T3 cells (murine fibroblast cell line) show no obvious response after introducing PMA. Moreover, the amounts of H_2O_2 released from different cells are calculated in Fig. 7c, and per Hela, MDA-MB-231 and MCF-7 produces 1.38×10^{-14}, 2.65×10^{-14} and 5.13×10^{-14} mol H_2O_2, respectively. MCF-7 cells exhibit the highest intracellular H_2O_2 level, consistent with previous reports [40]. Obviously, the $Mo_{0.75}W_{0.25}S_2$ based electrochemical biosensor can discriminate normal cells and different types of cancer cells accroding to their H_2O_2 concentration, which is of great importance in biosensing or other biological fields.

3.3. Electrocatalytic HER on $Mo_{1-x}W_xS_2$

The $Mo_{1-x}W_xS_2$ nanoflowers not only offer a sensitive platform for H_2O_2 detection, but also can be used in a variety of electrochemical reactions, such as HER. The MoS_2 and $Mo_{1-x}W_xS_2$ were investigated in 0.5 M H_2SO_4 (Fig. 8). The polarization curves identify that the $Mo_{0.75}W_{0.25}S_2$ only requires a overpotential (η_{10}) of 224 mV to achieve a current density of -10 mA cm^{-2} (Fig. 8a), which is lower than that of MoS_2 and other $Mo_{1-x}W_xS_2$. Accordingly, the $Mo_{0.75}W_{0.25}S_2$ delivers a lower Tafel slope of 56 mV dec^{-1}, indicating rapidly increasing H_2 generation rate with applied overpotential. This is consistent with its polarization curve (Fig. 8b). The higher slopes observed on the MoS_2 and other $Mo_{1-x}W_xS_2$ indicate the relatively slower kinetics. In further comparison with previously reported TMDs, e.g., rGO/WS_2 (η_{10}: 229 mV, Tafel slope: 73 mV dec^{-1}) [41], H_2-annealed MoS_2 (η_{10}: 357 mV, Tafel slope: 75 mV dec^{-1}) [42], bimetallic Co-doped MoS_2 nanofibers (η_{10}: 330 mV, Tafel slope: 60 mV dec^{-1}) [43] and W_xCo_yS (η_{10}: 228 mV, Tafel slope: 111 mV dec^{-1}) [44], the $Mo_{0.75}W_{0.25}S_2$ highlights the outstanding HER activity. The enhanced electrocatalytic performance should be ascribed to the engineered electronic configuration on edges. And the $Mo_{0.75}W_{0.25}S_2$ affords satisfactory stability for the HER in 0.5 M H_2SO_4 (Fig. 8c). There is negligible degradation observed in final polarization curves after 1000 continuous scans.

4. Conclusions

A series of bimetallic $Mo_{1-x}W_xS_2$ are fabricated and investigated as efficient electrochemical biosensors, with clearly evidenced composition-dependence on engineered electronic configurations and surface *OH binding. The optimal $Mo_{0.75}W_{0.25}S_2$ affords high sensitivity (1290 μA mM^{-1} cm^{-2}), good selectivity, and wide applicable concentration range (4×10^{-1}–1.0×10^4 μM), in comparison with single-component counterparts and even recently reported materials involving enzymes or precious metals. Owing the sensitive and specific H_2O_2 detection, the $Mo_{0.75}W_{0.25}S_2$ can distinguish normal cells and different cancer cells via monitoring the amount of endogenous H_2O_2. Moreover, it also accomplishes a high efficiency in electrocatalytic HER, highlighting the universal promotion in sensing and electrocatalysis that share similar electrochemical fundamentals. We believe that the more-precise manipulation on the composition and surface architecture of bimetallic TMDs will further boost their performance for both sensing and catalysis.

CRediT authorship contribution statement

Yijin Shu: Methodology, Investigation, Writing - original draft. **Wenbiao Zhang:** Software, Investigation. **Xing Yin:** Formal analysis. **Lingli Zhang:** Data curation. **Yang Yang:** Resources. **Dong Ma:** Writing - review & editing. **Qingsheng Gao:** Conceptualization, Supervision, Writing - review & editing.

Declaration of Competing Interest

The authors declare that they have no known competing financial interests or personal relationships that could have appeared to influence the work reported in this paper.

Acknowledgments

The authors appreciate the financial support from National Natural Science Foundation of China (grant No.: 21773093), Guangdong Natural Science Funds for Distinguished Young Scholar (grant No.: 2015A030306014), and Guangzhou Science and Technology Program (grant No.: 201707010268).

Appendix A. Supplementary material

Supplementary data to this article can be found online at https://doi.org/10.1016/j.jcis.2020.01.083.

References

[1] G. Maduraiveeran, M. Sasidharan, V. Ganesan, Electrochemical sensor and biosensor platforms based on advanced nanomaterials for biological and biomedical applications, Biosens. Bioelectron. 103 (2018) 113–129.
[2] S.N. Topkaya, M. Azimzadeh, M. Ozsoz, Electrochemical biosensors for cancer biomarkers detection: recent advances and challenges, Electroanalysis 28 (2016) 1402–1419.
[3] N.J. Ronkainen, H.B. Halsall, W.R. Heineman, Electrochemical biosensors, Chem. Soc. Rev. 39 (2010) 1747–1763.
[4] Y.F. Dai, C.C. Liu, Recent advances on electrochemical biosensing strategies toward universal point-of-care systems, Angew. Chem. Int. Ed. (2019) 12355–12368.
[5] R. Eivazzadeh-Keihan, P. Pashazadeh-Panahi, B. Baradaran, A. Maleki, M. Hejazi, A. Mokhtarzadeh, M. de la Guardia, Recent advances on nanomaterial based electrochemical and optical aptasensors for detection of cancer biomarkers, Trends Anal. Chem. 100 (2018) 103–115.
[6] N. Smirnoff, D. Arnaud, Hydrogen peroxide metabolism and functions in plants, New Phytol. 221 (2019) 1197–1214.
[7] X.M. Chen, G.H. Wu, Z.X. Cai, M. Oyama, X. Chen, Advances in enzyme-free electrochemical sensors for hydrogen peroxide, glucose, and uric acid, Microchim. Acta 181 (2014) 689–705.
[8] D.R. Gough, T.G. Cotter, Hydrogen peroxide: a jekyll and hyde signalling molecule, Cell Death Dis. 2 (2011) e213.
[9] J.J. Li, W.D. Ke, L. Wang, M.M. Huang, W. Yin, P. Zhang, Q.X. Chen, Z.S. Ge, Self-sufficing H_2O_2-responsive nanocarriers through tumor-specific H_2O_2 production for synergistic oxidation-chemotherapy, J. Contr. Release 225 (2016) 64–74.
[10] Q.H. Guan, L.L. Shi, C.T. Li, X.H. Gao, K. Wang, X.F. Liang, P.Y. Li, X.Y. Zhu, A fluorescent cocktail strategy for differentiating tumor, inflammation, and normal cells by detecting mRNA and H_2O_2, ACS Biomater. Sci. Eng. 5 (2019) 1023–1033.
[11] K. Dhara, D.R. Mahapatra, Recent advances in electrochemical nonenzymatic hydrogen peroxide sensors based on nanomaterials: a review, J. Mater. Sci. 54 (2019) 12319–12357.
[12] H.Y. Liu, L.Y. Weng, C. Yang, A review on nanomaterial-based electrochemical sensors for H_2O_2, H_2S and NO inside cells or released by cells, Microchim. Acta 184 (2017) 1267–1283.
[13] W. Chen, S. Cai, Q.-Q. Ren, W. Wen, Y.-D. Zhao, Recent advances in electrochemical sensing for hydrogen peroxide: a review, Analyst 137 (2012) 49–58.
[14] Y.H. Wang, K.J. Huang, X. Wu, Recent advances in transition-metal dichalcogenides based electrochemical biosensors: a review, Biosens. Bioelectron. 97 (2017) 305–316.
[15] R.N. Dalila, M.K.M. Arshad, S.C.B. Gopinath, W.M.W. Norhaimi, M.F.M. Fathil, Current and future envision on developing biosensors aided by 2D molybdenum disulfide (MoS_2) productions, Biosens. Bioelectron. 132 (2019) 248–264.
[16] V. Yadav, S. Roy, P. Singh, Z. Khan, A. Jaiswal, 2D MoS_2-based nanomaterials for therapeutic, bioimaging, and biosensing applications, Small 15 (2019) 1803706.
[17] M. Chhowalla, H.S. Shin, G. Eda, L.J. Li, K.P. Loh, H. Zhang, The chemistry of two-dimensional layered transition metal dichalcogenide nanosheets, Nat. Chem. 5 (2013) 263–275.

[18] K. Kalantar-zadeh, J.Z. Ou, Biosensors based on two-dimensional MoS_2, ACS Sensors 1 (2016) 5–16.
[19] X.R. Gan, H.M. Zhao, X. Quan, Two-dimensional MoS_2: a promising building block for biosensors, Biosens. Bioelectron. 89 (2017) 56–71.
[20] Y. Guo, Y. Shu, A. Li, B. Li, J. Pi, J. Cai, H.-H. Cai, Q. Gao, Efficient electrochemical detection of cancer cells on in situ surface-functionalized MoS_2 nanosheets, J. Mater. Chem. B 5 (2017) 5532–5538.
[21] A. Gupta, T.B. Rawal, C.J. Neal, S. Das, T.S. Rahman, S. Seal, Molybdenum disulfide for ultra-low detection of free radicals: electrochemical response and molecular modeling, 2D Materials 4 (2017) 025077.
[22] T. Wang, H. Zhu, J. Zhuo, Z. Zhu, P. Papakonstantinou, G. Lubarsky, J. Lin, M. Li, Biosensor based on ultrasmall MoS_2 nanoparticles for electrochemical detection of H_2O_2 released by cells at the nanomolar level, Anal. Chem. 85 (2013) 10289–10295.
[23] Y.J. Shu, W.B. Zhang, H.H. Cai, Y. Yang, X. Yu, Q.S. Gao, Expanding the interlayers of molybdenum disulfide toward the highly sensitive sensing of hydrogen peroxide, Nanoscale 11 (2019) 6644–6653.
[24] D.Z. Zhang, J.F. Wu, P. Li, Y.H. Cao, Room-temperature SO_2 gas-sensing properties based on a metal-doped MoS_2 nanoflower: an experimental and density functional theory investigation, J. Mater. Chem. A 5 (2017) 20666–20677.
[25] D. Geng, X.J. Bo, L.P. Guo, Ni-doped molybdenum disulfide nanoparticles anchored on reduced graphene oxide as novel electroactive material for a non-enzymatic glucose sensor, Sensor. Actuat. B Chem. 244 (2017) 131–141.
[26] H. Giang, M. Pali, L. Fan, Suni, II, Impedance biosensing atop MoS_2 thin films with Mo-S bond formation to antibody fragments created by disulphide bond reduction, Electroanalysis 31 (2019) 957–965.
[27] D. Sarkar, X.J. Xie, J.H. Kang, H.J. Zhang, W. Liu, J. Navarrete, M. Moskovits, K. Banerjee, Functionalization of transition metal dichalcogenides with metallic nanoparticles: implications for doping and gas-sensing, Nano Lett. 15 (2015) 2852–2862.
[28] X.J. Liu, L.P. Li, Y.J. Wei, Y.Z. Zheng, Q. Xiao, B. Feng, Facile synthesis of boron- and nitride-doped MoS_2 nanosheets as fluorescent probes for the ultrafast, sensitive, and label-free detection of Hg^{2+}, Analyst 140 (2015) 4654–4661.
[29] H. Wang, L.Y. Ouyang, G.F. Zou, C. Sun, J. Hu, X. Xiao, L.J. Gao, Optimizing MoS_2 edges by alloying isovalent W for robust hydrogen evolution activity, ACS Catal. 8 (2018) 9529–9536.
[30] A.F. Rigosi, H.M. Hill, K.T. Rim, G.W. Flynn, T.F. Heinz, Electronic band gaps and exciton binding energies in monolayer $Mo_xW_{1-x}S_2$ transition metal dichalcogenide alloys probed by scanning tunneling and optical spectroscopy, Phys. Rev. B 94 (2016) 075440.
[31] Perdew, Burke, Wang, Generalized gradient approximation for the exchange-correlation hole of a many-electron system, Phys. Rev. B 54 (1996) 16533–16539.
[32] W. Zhang, G.Z. Fan, H. Yi, G. Jia, Z.S. Li, C.W. Yuan, Y.F. Bai, D.G. Fu, Interfacial engineering of hierarchical transition metal oxide heterostructures for highly sensitive sensing of hydrogen peroxide, Small 14 (2018) 1703713.
[33] M.-R. Gao, M.K.Y. Chan, Y. Sun, Edge-terminated molybdenum disulfide with a 9.4-angstrom interlayer spacing for electrochemical hydrogen production, Nat. Commun. 6 (2015) 7493.
[34] K.H. Liu, L.M. Zhang, T. Cao, C.H. Jin, D.A. Qiu, Q. Zhou, A. Zettl, P.D. Yang, S.G. Louie, F. Wang, Evolution of interlayer coupling in twisted molybdenum disulfide bilayers, Nat. Commun. 5 (2014) 4966.
[35] G.C. Wang, L. Li, W.H. Fan, R.Y. Wang, S.S. Zhou, J.T. Lue, L. Gan, T.Y. Zhai, Interlayer coupling induced infrared response in WS_2/MoS_2 heterostructures enhanced by surface plasmon resonance, Adv. Funct. Mater. 28 (2018) 1800339.
[36] H.Q. Gong, F. Zheng, Z. Li, Y. Li, P.F. Hu, Y. Gong, S.L. Song, F.Y. Zhan, Q. Zhen, Hydrothermal preparation of MoS_2 nanoflake arrays on Cu foil with enhanced supercapacitive property, Electrochim. Acta 227 (2017) 101–109.
[37] D.M. Hou, W.J. Zhou, X.J. Liu, K. Zhou, J. Xie, G.Q. Li, S.W. Chen, Pt nanoparticles/MoS_2 nanosheets/carbon fibers as efficient catalyst for the hydrogen evolution reaction, Electrochim. Acta 166 (2015) 26–31.
[38] Y.D. Hou, Y.S. Zhu, Y. Xu, X.C. Wang, Photocatalytic hydrogen production over carbon nitride loaded with WS_2 as cocatalyst under visible light, Appl. Catal. B: Environ. 156 (2014) 122–127.
[39] R.R. Kharade, S.S. Mali, S.P. Patil, K.R. Patil, M.G. Gang, P.S. Patil, J.H. Kim, P.N. Bhosale, Enhanced electrochromic coloration in Ag nanoparticle decorated WO_3 thin films, Electrochim. Acta 102 (2013) 358–368.
[40] M. Mohammadniaei, J. Yoon, T. Lee, B.G. Bharate, J. Jo, D. Lee, J.W. Choi, Electrochemical biosensor composed of silver ion-mediated dsDNA on Au-encapsulated Bi_2Se_3 nanoparticles for the detection of H_2O_2 released from breast cancer cells, Small 14 (2018) 1703970.
[41] T.A. Shifa, F. Wang, Z. Cheng, X. Zhan, Z. Wang, K. Liu, M. Safdar, L. Sun, J. He, A vertical-oriented WS_2 nanosheet sensitized by graphene: an advanced electrocatalyst for hydrogen evolution reaction, Nanoscale 7 (2015) 14760–14765.
[42] M. He, F. Kong, G. Yin, Z. Lv, X. Sun, H. Shi, B. Gao, Enhanced hydrogen evolution reaction activity of hydrogen-annealed vertical MoS_2 nanosheets, RSC Adv. 8 (2018) 14369–14376.
[43] Y. Rheem, S.H. Park, Y. Han, K.-H. Lee, S.-M. Choi, N.V. Myung, Electrospun cobalt-doped MoS_2 nanofibers for electrocatalytic hydrogen evolution, J. Electrochem. Soc. 166 (2019) F996–F999.
[44] F. Wang, L. Xu, P. Wang, Y. Zhang, W_xCo_yS core-shell grown on hollow-porous carbon fiber (HCF) as synergetic electrocatalysts for efficient water splitting, Electrochim. Acta 306 (2019) 437–445.